

Impact of crust-core connection procedures on the tidal deformability of neutron stars

Junbo Pang¹, Hong Shen¹*, and Jinniu Hu¹†
¹ School of Physics, Nankai University, Tianjin 300071, China

We study the impact of crust-core connection procedures on various neutron-star properties, especially on the tidal deformability. We consider three types of connection procedures to treat the discontinuity in a nonunified equation of state around the crust-core transition: (1) the direct connection procedure, (2) the crossover connection procedure, and (3) the segmented method. Our results indicate that the mass-radius relations of neutron stars are almost unaffected by the details of the connection procedure. However, the tidal deformabilities of neutron stars are sensitive to the crust-core connection procedures. The tidal deformability is closely related to gravitational-wave measurements. For a canonical $1.4M_{\odot}$ neutron star, uncertainties in the tidal deformability $\Lambda_{1.4}$ from different connection procedures can exceed 20%. We find that the direct connection procedure yields significantly larger uncertainties in the tidal deformability, while the segmented method and crossover connection procedure provide relatively stable results.

I. INTRODUCTION

Neutron stars are natural laboratories for studying the equation of state (EOS) of dense matter under extreme conditions. Over the past decades, astronomical observational technologies have achieved significant improvements, which have greatly improved our measurements and understanding of neutron-star properties, such as the mass, radius, and internal features [1–3]. These observations provide a wealth of information for constraining physics of matter under extreme conditions. Furthermore, the first direct detection of gravitational waves from a binary black hole merger, known as GW150914 [4], launched a new era of gravitational-wave astronomy. The observations of compact binary mergers by the LIGO and Virgo detectors have provided valuable constraints on the neutron star EOS and its underlying theoretical framework. It is well known that the tidal deformability of neutron stars can be inferred from gravitational-wave observations, although large uncertainty remains from both the measurements and theoretical analyses. The milestone gravitational wave event GW170817 [5, 6] from a binary neutron-star merger provided an estimate of the tidal deformability and constrained the radius for canonical neutron stars with masses around $1.4M_{\odot}$ [7–10]. In addition, several precise measurements for massive pulsars, PSR J1614-2230 ($1.908 \pm 0.016M_{\odot}$) [11], PSR J0348+0432 ($2.01 \pm 0.04M_{\odot}$) [12], and PSR J0740+6620 ($2.08 \pm 0.07M_{\odot}$) [13], require the predicted maximum neutron-star mass to be larger than $2M_{\odot}$, which makes a stringent constraint on the EOS of neutron stars. The recent observations by NICER (Neutron Star Interior Composition Explorer) for PSR J0030+0451 [14, 15] and PSR J0740+6620 [16, 17] provided simultaneous measurements of the mass and radius of neutron stars, which offer further constraints on the EOS of dense matter.

The EOS plays a decisive role in studying various properties of neutron stars [18–20]. The EOS used as input for calculating neutron-star structure generally covers a wide density

range, which includes three segments: (a) the EOS of the outer crust below the neutron drip density; (b) the EOS of the inner crust from neutron drip to crust-core transition; (c) the EOS of the liquid core above the crust-core transition. The outer crust extends from the surface of the star to the neutron drip density, which is composed of spherical nuclei and a background of relativistic electron gas. The behavior of the outer crust is primarily determined by experimental nuclear masses, so there are no significant differences in the EOS of the outer crust when using different nuclear-mass models [18]. As the density increases, neutrons drip out of nuclei and form a dilute neutron gas along with the electron gas in the inner crust. When the density increases toward the crust-core transition, spherical nuclei may become unstable and nuclear shapes may vary, known as nuclear pasta phases [21–23]. The transition from the inner crust to the core, referred to as the crust-core transition, occurs at about $1/3$ to $1/2$ nuclear saturation density, depending on the nuclear models. The uniform matter in the core includes neutrons, protons, electrons, and muons under β equilibrium, extending from the crust-core transition up to a few times the nuclear saturation density. The possible appearance of non-nucleonic degrees of freedom in the dense interior of neutron stars has been widely discussed in review papers [19, 20, 24]. When the electron chemical potential becomes sufficiently high, negatively charged mesons such as π^- and K^- may appear in the ground state, forming boson condensation inside neutron stars. The possibility of pion condensation [25, 26] and antikaon condensation [27–29] has been investigated within various approaches. Other particles, such as hyperons and quarks, may appear and soften the EOS at higher densities [30–34]. The appearance of these exotic components generally causes a significant reduction of the maximum neutron-star mass [35–38]. For simplicity, we do not include the non-nucleonic degrees of freedom in the present study.

The mass and radius of a neutron star are essentially determined by the high-density core EOS, which should connect to the inner crust EOS at the crust-core transition. When the core and crust EOSs are obtained within the same nuclear model, the transition density can be consistently determined, and such an EOS is known as a unified EOS. There have been

* shennankai@gmail.com
† hujinniu@nankai.edu.cn

some studies aimed at developing a unified EOS [39–45]. The use of a unified EOS is important for investigating the crust–core transition and detailed properties of neutron stars. However, most studies on neutron stars, for simplicity, employ a nonunified EOS and pay much more attention to the core EOS. A nonunified EOS involves a core EOS that is matched to a commonly used crust EOS obtained from different models [44, 45]. Such matching may introduce a discontinuity in the nonunified EOS around the crust–core transition, potentially leading to uncertainties in the predictions of tidal deformability and other neutron-star properties. It has been reported in Ref. [44] that the crust–core connection procedure could slightly affect the resulting radius and crust thickness of neutron stars. Generally, it is considered that the crust EOS has less effect on the global properties of neutron stars, but it may influence the resulting tidal deformabilities [45]. Furthermore, the crust–core connection procedure in a nonunified EOS may also affect the resulting tidal deformabilities.

Our aim in this study is to quantitatively analyze the impact of the EOS connection at the crust–core transition point on tidal deformability. Moreover, we intend to propose a segmented method, which has low uncertainty in calculating neutron-star properties and helps avoid misleading results in studies of tidal deformability. For this purpose, we considered three types of connection procedures to treat the discontinuity around the crust–core transition. The first one, i.e., the direct connection procedure, adopts the Newton polynomial interpolation method [46] to directly connect the inner crust and core segments. The second one, i.e., the crossover connection procedure, employs a regularized calculation [47] to generate a crossover EOS between the inner crust and core segments. The third one, i.e., the segmented method, solves the Tolman–Oppenheimer–Volkoff (TOV) equation separately inside the crust and core regions, while appropriate matching conditions are imposed at the crust–core interface [48].

To simplify the analysis of results, we adopt specific core and crust segments. The core EOS is obtained within the relativistic mean-field (RMF) model using the TM1e [45], BigApple [49], and IUFSU [50] parameterizations. Over the past decades, the RMF approach based on various energy density functionals has been successfully applied to the description of finite nuclei and infinite nuclear matter [51]. The BigApple model, proposed by Fattoyev et al. [49] after the discovery of GW190814, incorporates various constraints from astrophysical observations as well as the ground-state properties of finite nuclei. The inner crust EOS is based on the self-consistent Thomas–Fermi approximation within the RMF model using the TM1e and TM1 parametrizations [45, 52], which has been shown to be compatible with the constraints from astrophysical observations and various properties of finite nuclei [53]. We note that the TM1e and TM1 models have significantly different behaviors of nuclear symmetry energy. The slope parameters of symmetry energy are respectively $L = 40$ MeV (TM1e) and $L = 111$ MeV (TM1). The difference in L plays a key role in the crust–core transition of neutron stars [45, 54]. Accordingly, different combinations of the inner crust and core EOSs yield different behaviors at the crust–core interface. For the outer crust below the neutron drip

density, we employ the well-known Baym–Pethick–Sutherland (BPS) EOS [55], which has a relatively small influence on the neutron-star properties considered here. In the present work, we focus on the uncertainty in tidal deformability induced by the crust–core connection procedure in a neutron star.

This article is organized as follows. In Sec. II, we briefly describe the TOV equation for neutron-star calculations and the interpolation method for constructing the EOS. In Sec. III, we investigate the impact of the crust–core connection procedures on neutron-star properties and discuss the results, making a detailed comparison among the three types of connection procedures considered in this work. Finally, a summary and conclusions are presented in Sec. IV.

II. FORMALISM

In this section, we first describe the calculation for neutron-star properties, such as the tidal deformability, and then describe the construction of the EOS including the crust–core connection methods.

A. Neutron-star properties

The neutron-star properties, such as the gravitational mass (M) and the radius (R), can be obtained by solving the TOV equation [56] (in units of $G = c = 1$)

$$\begin{aligned} \frac{dP(r)}{dr} &= -\frac{M(r)\varepsilon(r)}{r^2} \left[1 + \frac{P(r)}{\varepsilon(r)} \right] \\ &\quad \times \left[1 + \frac{4\pi r^3 P(r)}{M(r)} \right] \left[1 - \frac{2M(r)}{r} \right]^{-1}, \\ \frac{dM(r)}{dr} &= 4\pi r^2 \varepsilon(r), \end{aligned} \quad (1)$$

where $P(r)$ and $\varepsilon(r)$ are the pressure and energy density at the radial coordinate r , respectively. $M(r)$ is the gravitational mass enclosed within the radius r . The dimensionless tidal deformability Λ of neutron stars is expressed as [57]

$$\Lambda = \frac{2}{3}k_2C^{-5}, \quad (2)$$

with the compactness parameter given by $C = M/R$. The second tidal Love number k_2 is calculated from [48]

$$\begin{aligned} k_2 &= \frac{8C^5}{5} (1 - 2C)^2 [2 - y_R + 2C(y_R - 1)] \\ &\quad \times \{2C [6 - 3y_R + 3C(5y_R - 8)] \\ &\quad + 4C^3 [13 - 11y_R + C(3y_R - 2) + 2C^2(1 + y_R)] \\ &\quad + 3(1 - 2C)^2 [2 - y_R + 2C(y_R - 1)] \\ &\quad \times \ln(1 - 2C)\}^{-1}, \end{aligned} \quad (3)$$

where $y_R = y(r)|_{r=R}$ is obtained by solving the following differential equation,

$$\frac{dy(r)}{dr} = -\frac{1}{r} [y(r)^2 + y(r)F(r) + r^2Q(r)], \quad (4)$$

with

$$F(r) = \left\{ 1 - 4\pi r^2 [\varepsilon(r) - P(r)] \right\} \left[1 - \frac{2M(r)}{r} \right]^{-1},$$

$$Q(r) = \left\{ 4\pi \left[5\varepsilon(r) + 9P(r) + \frac{\varepsilon(r) + P(r)}{\partial P(r)/\partial \varepsilon(r)} \right] - \frac{6}{r^2} \right\} \times \left[1 - \frac{2M(r)}{r} \right]^{-1} - \left(\frac{2M(r)}{r^2} \right)^2 \left[1 + \frac{4\pi r^3 P(r)}{M(r)} \right]^2 \times \left[1 - \frac{2M(r)}{r} \right]^{-2}. \quad (5)$$

B. Extract energy density from EOS

The EOS, which is constructed under the conditions of β -equilibrium and charge neutrality, is a critical input for solving the TOV equation. Typically, the EOS inputted into the solving program is not a specific $P - \varepsilon$ function, but a set of discrete data points. Therefore, interpolation methods are necessary to obtain the energy density corresponding to any specific pressure value. In this work, the method we employ is based on Newton polynomial interpolation method [46], which ensures that the interpolation results do not deviate significantly from the polyline formed by connecting the discrete points of the input EOS. In this method, the energy density ε_i at a given pressure P_i is calculated by the following steps:

- (1) Locate P_i within the input EOS data table, and denote the three data points before and after it as

$$(P_1, \varepsilon_1), (P_2, \varepsilon_2), (P_3, \varepsilon_3), \\ (P_4, \varepsilon_4), (P_5, \varepsilon_5), (P_6, \varepsilon_6),$$

where P_i satisfies,

$$P_1 < P_2 < P_3 < P_i < P_4 < P_5 < P_6. \quad (6)$$

- (2) Calculate four interpolation values obtained from Newton formula,

$$f^{(2)}(P_i) = \sum_{m=3}^4 f[P_3, \dots, P_m] \prod_{n=3}^{m-1} (P_i - P_n),$$

$$f_L^{(4)}(P_i) = \sum_{m=1}^4 f[P_1, \dots, P_m] \prod_{n=1}^{m-1} (P_i - P_n), \quad (7)$$

$$f_C^{(4)}(P_i) = \sum_{m=2}^5 f[P_2, \dots, P_m] \prod_{n=2}^{m-1} (P_i - P_n),$$

$$f_R^{(4)}(P_i) = \sum_{m=3}^6 f[P_3, \dots, P_m] \prod_{n=3}^{m-1} (P_i - P_n),$$

where the divided difference $f[P_j, \dots, P_k]$ ($j \leq k$) is recursively defined by the equations

$$f[P_j] = \varepsilon_j, \\ f[P_j, \dots, P_k] = \frac{f[P_j, \dots, P_{k-1}] - f[P_{j+1}, \dots, P_k]}{P_j - P_k}. \quad (8)$$

The value of $f^{(2)}(P_i)$ actually employs only two data points, hence the interpolation polynomial is transformed into a linear function. Furthermore, we define:

$$\Delta_L = \left| \frac{f_L^{(4)}(P_i) - f^{(2)}(P_i)}{f^{(2)}(P_i)} \right|, \\ \Delta_C = \left| \frac{f_C^{(4)}(P_i) - f^{(2)}(P_i)}{f^{(2)}(P_i)} \right|, \\ \Delta_R = \left| \frac{f_R^{(4)}(P_i) - f^{(2)}(P_i)}{f^{(2)}(P_i)} \right|, \quad (9)$$

to characterize the difference between the interpolation results obtained by selecting different data points and the simple polyline of the input EOS data table.

- (3) The final value of ε_i is determined by the following conditions:
 - In the case of $\min [\Delta_L, \Delta_C, \Delta_R] > 10^{-3}$, the value of ε_i is taken directly from the linear interpolation to ensure that ε_i does not deviate significantly from the original polyline,

$$\varepsilon_i = f^{(2)}(P_i). \quad (10)$$

- In the case of $\min [\Delta_L, \Delta_C, \Delta_R] \leq 10^{-3}$, the value of ε_i is chosen to correspond to the minimum Δ ,

$$\varepsilon_i = f^{(4)}(\min [\Delta_L, \Delta_C, \Delta_R]). \quad (11)$$

To calculate the tidal deformability Λ by solving Eq. (4), the sound speed squared c_s^2 should be provided together with the energy density ε at a given pressure P . Prior to solving the equations, we build an input table that contains, for each pressure P , the corresponding energy density ε and sound speed squared c_s^2 computed from the numerical derivative $c_s^2 = \partial P/\partial \varepsilon$. Once the equations are solved, c_s^2 at any pressure P_i is determined using Newton interpolation, in the same way as ε_i , as described above.

III. RESULTS AND DISCUSSION

It is interesting to explore how the construction of EOS influences neutron-star properties. In nonunified EOSs, a discontinuity in energy density typically appears at the crust-core transition. Such a discontinuity may induce significant uncertainties in the resulting tidal deformability of neutron stars. Therefore, an appropriate connection procedure is required to ensure a smooth EOS across the transition region, so that the tidal deformability can be reliably determined. In the present work, we focus on the uncertainty in tidal deformability induced by the connection procedure at the crust-core interface of neutron stars.

In Fig. 1, we show the energy density ε as a function of the pressure P including the crust and core segments used in the

present study. The outer crust EOS is shown by the black solid line, and its matching point to the inner crust is marked by the black filled square. The inner crust EOSs from different models are distinguished by color. The pressure at each colored filled star, denoted as P_* , represents the maximum pressure at which the nonuniform matter can exist for each model. The core EOS consists of two segments, shown by a solid line and a dash-dotted line, joined at a colored filled triangle. When solving the TOV equation, the solid-line segment remains unchanged, while all connection procedures affect only the dash-dotted segment. The pressure at the colored filled triangle is denoted as P_Δ . This implies that the connection procedure modifies only the core segment with $P < P_\Delta$.

It is noteworthy that the exact location of the crust-core transition is uncertain in nonunified EOSs. Therefore, we adopt different connection procedures to investigate the influence of the crust-core connection on the tidal deformability of neutron stars. In this work, we employ three types of connection procedures:

- Direct connection. This procedure is applied above the critical pressure P_* . It fully retains the inner crust EOS up to P_* , where the nonuniform matter vanishes, and then directly connects to the core EOS. The connection is implemented over a narrow pressure interval, with a maximum range of $[P_*, P_\Delta]$, where Newton interpolation [46] is employed (Sec. III A).
- Crossover connection. This procedure is performed in the overlapping region of the inner crust and core segments. We employ a regularized calculation [47] to generate a crossover EOS between these two segments (Sec. III B).
- Segmented method. In this procedure, the TOV equa-

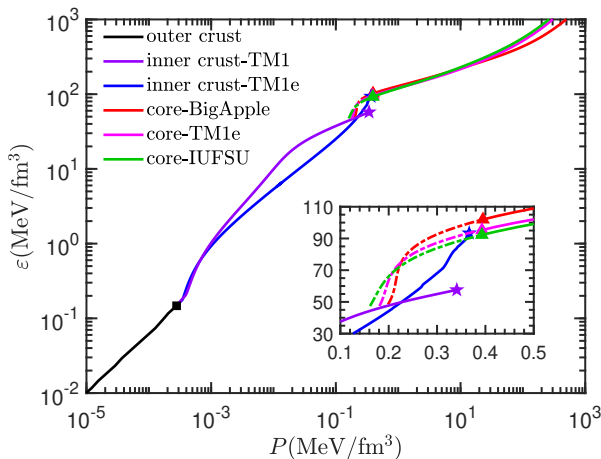


FIG. 1. The neutron-star matter EOSs used in this work. The energy density ε as a function of the pressure P includes three segments: outer crust, inner crust, and core, shown by different colors. The BPS EOS is adopted for the outer crust, and its matching point to the inner crust is marked by the black filled square. The end of the inner crust is marked by the colored filled stars. The colored filled triangles divide each core EOS into two segments. The connection procedure affects only the dash-dotted segments below the triangles.

tion is solved separately inside the crust and core [48]. Appropriate matching conditions are imposed at the connection pressure to ensure continuity and consistency between the two regions (Sec. III C).

A. Direct connection

We employ the direct connection procedure [44] in the pressure interval $[P_*, P_\Delta]$. In Fig. 2, we present the profiles for the three sets of nonunified EOSs, constructed by the direct connection procedure, using different combinations of the crust and core EOSs. All EOSs in Fig. 2 share a similar structure, consisting of three segments: the crust EOS, the connection region, and the core EOS. The connection region begins at the critical pressure P_* of each inner crust EOS and terminates at the chosen endpoint P_D . Consequently, the structure of the EOS can be represented as follows:

$$[\text{crust}] \xrightarrow{(P_*, \varepsilon_*)} [\text{connection}] \xrightarrow{(P_D, \varepsilon_D)} [\text{core}], \quad (12)$$

where D can be I, II, III, or Δ . The pressures P_I , P_{II} and P_{III} are the first, second, and third quartiles of the maximum connection interval $[P_*, P_\Delta]$ [see Fig. 2(a-1)]. As mentioned above, in numerical calculations, the EOS is derived from a polyline constructed from discrete data points. Within the connection region, there are only a finite number of these data points, which is denoted as n . By changing n and D , we carry out two types of connections:

Type1. We directly connect (P_*, ε_*) to (P_D, ε_D) , which means there is no extra data point in the connection region:

$$[\text{crust}] \parallel [(P_*, \varepsilon_*)] \parallel [core]. \quad (13)$$

In this case, $n = 0$ and $D = \text{I, II, III, } \Delta$.

Type2. We add n points to the connection region, where $n \geq 1$:

$$[\text{crust}] \parallel [(P_*, \varepsilon_*)] \parallel [A_1, \dots, A_n] \parallel [(P_D, \varepsilon_D)] \parallel [core]. \quad (14)$$

For $i = 1, \dots, n$, A_i denotes the added data point (P_i, ε_i) . The pressures corresponding to these n points are the equally spaced points within the connection region, which is given by

$$P_i = P_* + \frac{i}{n+1} (P_D - P_*). \quad (15)$$

The corresponding energy density ε_i is obtained via four-point Newton interpolation based on the points (P_*, ε_*) , (P_D, ε_D) , and the two closest higher-pressure data points.

Based on these connection methods, we construct three sets of EOS for each combination of crust and core EOSs, as shown in the top ($n = 0$), middle ($n = 1$), and bottom ($n = 2$) panels of Fig. 2. It is interesting to examine how sensitive the properties of neutron stars, such as the mass-radius relation and tidal deformability, are to the connection procedure.

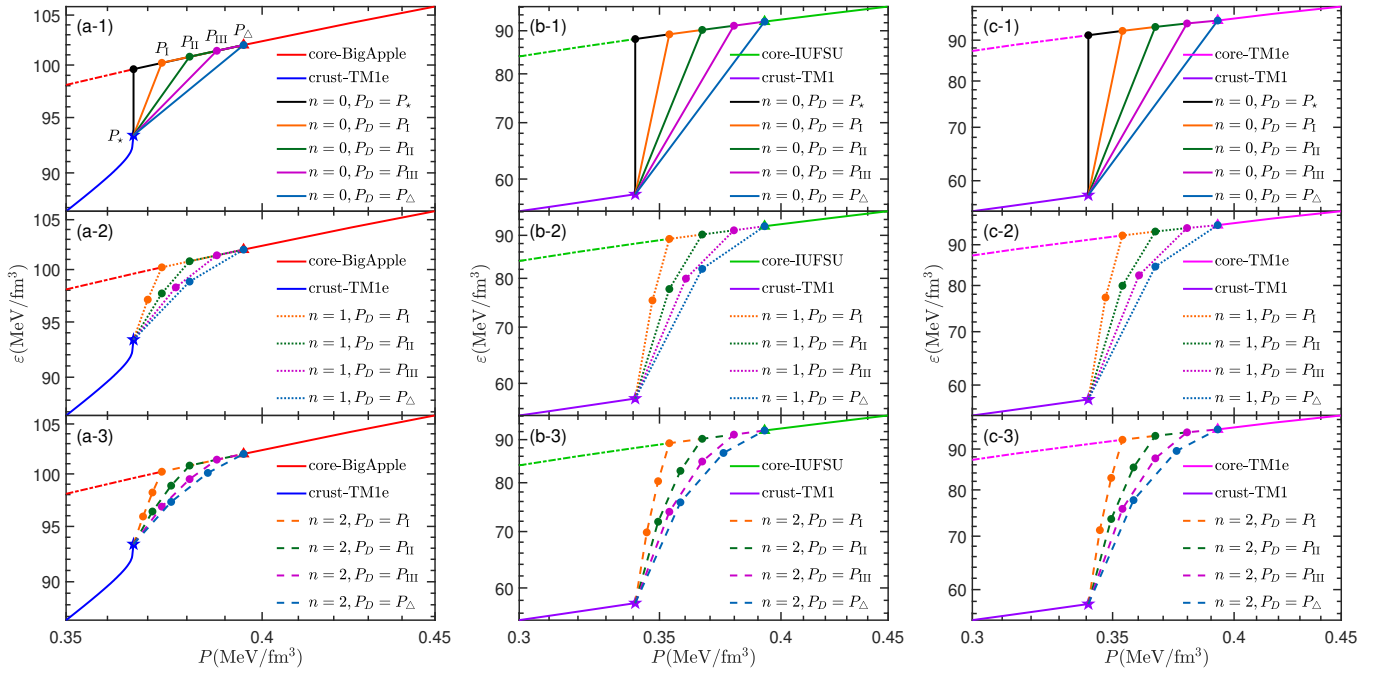


FIG. 2. Profiles for all nonunified EOSs constructed by the direct connection procedure. (a) shows the results for the combination of BigApple (core) + TM1e (crust). (b) is for IUFSU (core) + TM1 (crust). (c) is for TM1e (core) + TM1 (crust).

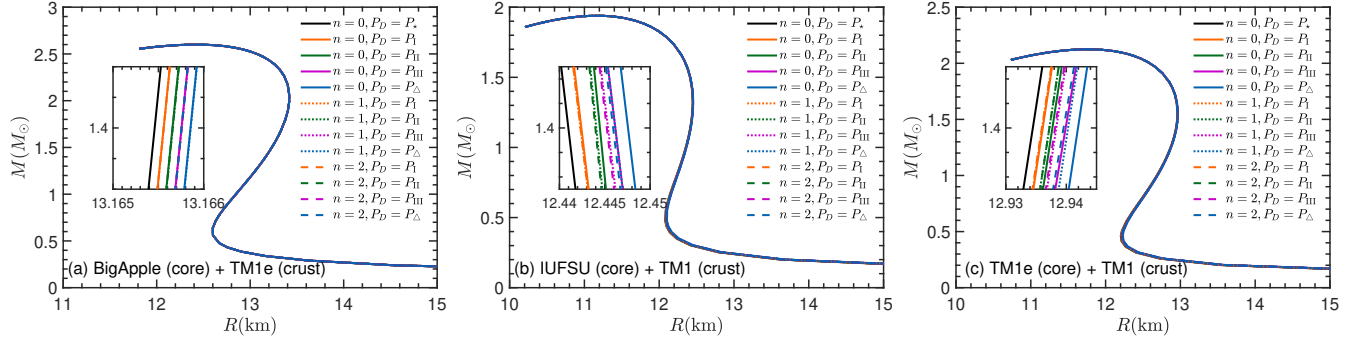


FIG. 3. Mass-radius relations predicted by the direct-connection EOSs shown in Fig. 2. The insets show more details for canonical neutron stars with masses around $1.4 M_{\odot}$.

In Fig. 3, we show the mass-radius relations obtained using these EOSs. It is seen that, for each combination, the mass-radius relations obtained with different P_D and n are almost indistinguishable. There are very tiny variations for the radii of canonical $1.4 M_{\odot}$ neutron stars, as shown in the insets. For the combination (a) BigApple (core) + TM1e (crust), the maximum difference in the radius of a $1.4 M_{\odot}$ neutron star ($R_{1.4}$) is less than 10^{-3} km. For the other two combinations, the maximum difference in $R_{1.4}$ does not exceed 10^{-2} km. This implies that the differences in the crust-core connections, as illustrated in Fig. 2, have a negligible impact on the mass-radius relations of neutron stars. However, the influence of the crust-core connections on the tidal deformability of neutron stars may be noticeable.

In Fig. 4(a-1), (b-1), (c-1), the tidal Love number k_2 is shown as a function of the neutron-star mass M , using the EOSs presented in Fig. 2. It is seen that the values of k_2 in-

crease with M , reach a maximum value around $0.8-1.0 M_{\odot}$, and then decrease as M continues to increase until reaching the maximum mass. The details shown in the insets indicate that variations in the crust-core connections do affect the values of k_2 for canonical neutron stars with masses around $1.4 M_{\odot}$. It is found that the values of k_2 increase with increasing n and P_D . Similar behaviors are also observed in the tidal deformability, Λ , plotted in Fig. 4(a-2), (b-2), (c-2). As shown in the insets, the variations in the crust-core connections lead to noticeable differences in the tidal deformability of a $1.4 M_{\odot}$ neutron star ($\Lambda_{1.4}$). The maximum difference in $\Lambda_{1.4}$ is approximately 35 for the combination of BigApple (core) + TM1e (crust), and about 50 and 80 for IUFSU (core) + TM1 (crust) and TM1e (core) + TM1 (crust), respectively. These results show that when no additional data points are introduced into the connection region, the tidal deformability is sensitive to the choice of P_D . By adding extra data points to

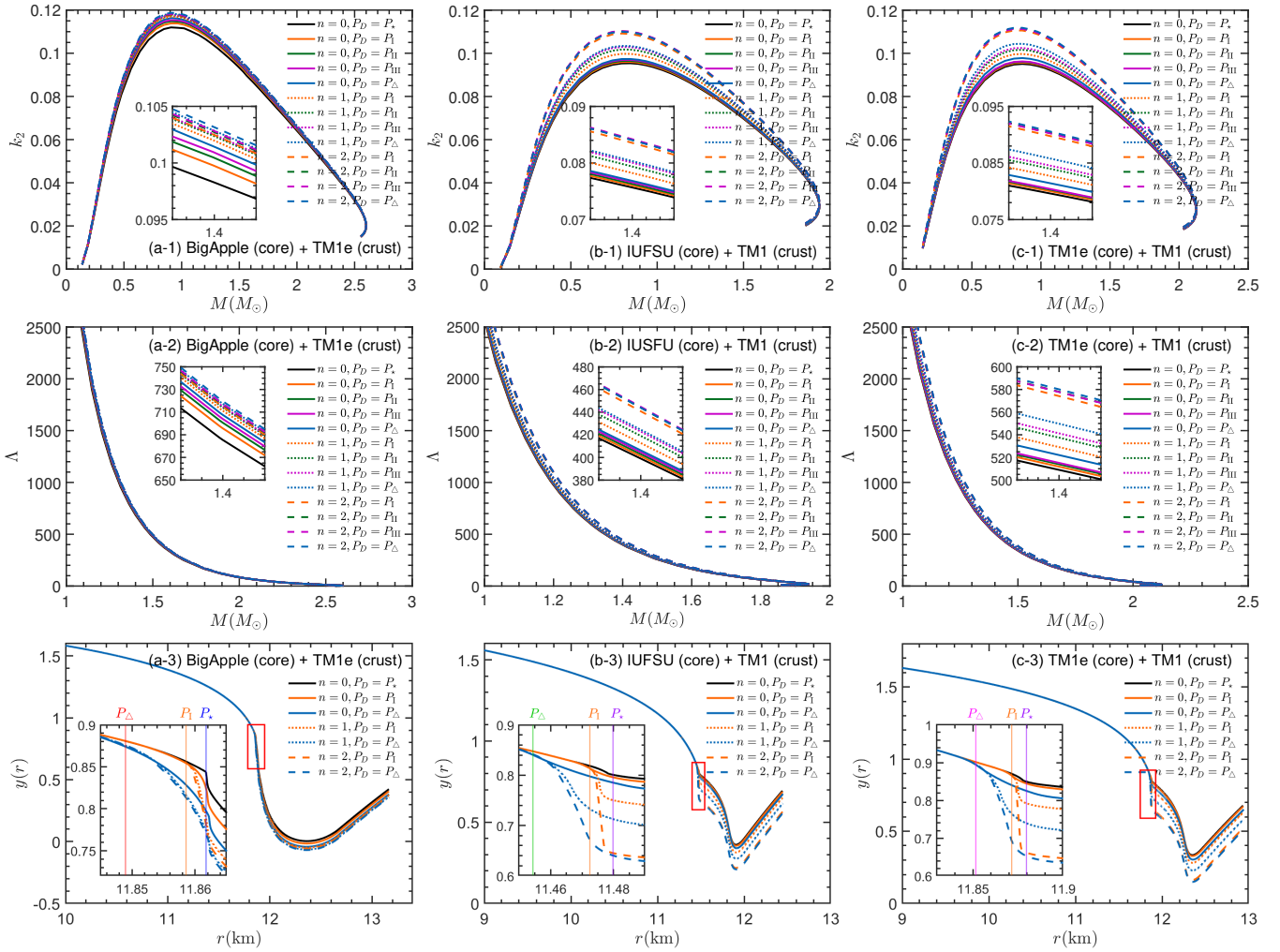


FIG. 4. (a,b,c-1) Love number k_2 and (a,b,c-2) tidal deformability Λ as a function of the neutron-star mass M predicted by the direct-connection EOSs shown in Fig. 2. The insets show more details for canonical neutron stars with masses around $1.4 M_\odot$. (a,b,c-3) The $y(r)$ profiles as given in Eq. (4) for a $1.4 M_\odot$ neutron star. The insets show the results in the direct connection region. The pressures corresponding to the vertical lines are consistent with those in Fig. 2.

the connection region, the sensitivity to P_D can be reduced, while these differences are still visible (see Table I, II, II). Because the variations in P_D and n do not cause significant changes in the mass-radius relation, the compactness C is consequently insensitive to these connections. Therefore, the differences in $\Lambda_{1.4}$ are mainly attributed to variations in k_2 , as described in Eq. (2). According to Eq. (3), the value of k_2 is determined by the compactness parameter C and the value of y_R . Consequently, the differences in k_2 should be attributed to varying behaviors of y_R . In Fig. 4(a-3), (b-3), (c-3), we plot several profiles of $y(r)$ for a $1.4 M_\odot$ neutron star. It is seen that $y(r)$, as a function of the radial coordinate r , decreases smoothly in the core region and varies rapidly beyond the crust-core interface, which is indicated by the red rectangle. The value of $y(r)$ reaches a minimum inside the crust and then increases until reaching the neutron-star surface at radius R , where y_R is the value of $y(r)$. Taking the combination of BigApple (core) + TM1e (crust) as an example, all curves in Fig. 4(a-3) are almost identical for $r < 11.85$ km, because of

the same core EOS applied in the calculations at this stage. However, due to the variations in the crust-core connections, for $r > 11.85$ km, differences among the curves can be observed and gradually become more visible, eventually leading to significantly different values of y_R . To investigate the effects of different crust-core connections on y_R , we show the details near the crust-core interface in the inset of Fig. 4(a-3). The vertical lines in different colors indicate that the pressure at $r = r_D$ satisfies $P|_{r=r_D} = P_D$. All calculations in this case employ the TM1e crust EOS for $r > r_*$. When no additional data points are added with $n = 0$, we find that as P_D increases from P_* to P_Δ , the values of $y(r)$ in the crust-core connection region are in decreasing order. Eventually, different values of y_R are obtained. This implies that the differences in y_R are mainly attributed to different P_D used. When additional data points are added in the cases of $n = 1$ and $n = 2$, the values of $y(r)$ in the crust-core connection region are significantly reduced. Comparison of the results for $n = 0$ to those for $n = 1$ and $n = 2$ shows that the differences in $y(r)$ curves

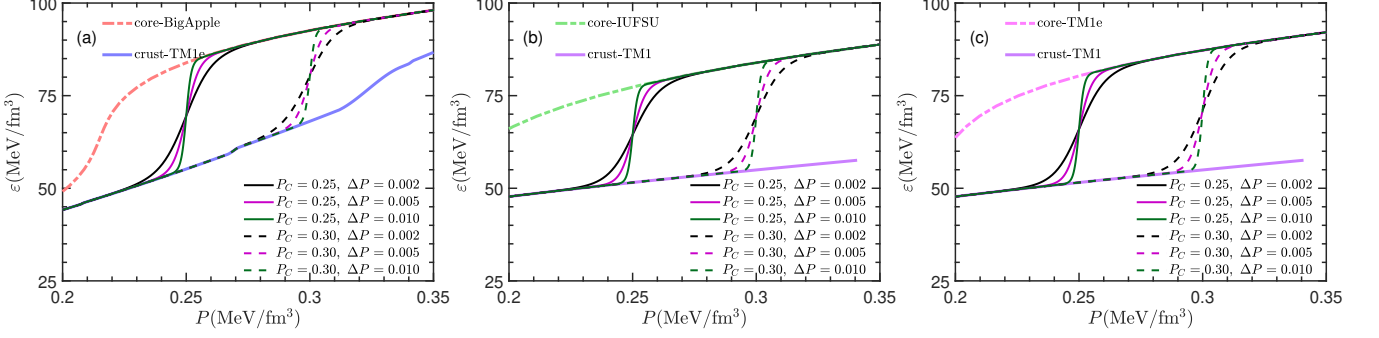


FIG. 5. Profiles of the crossover-connection EOSs. (a) shows the results for the combination of BigApple (core) + TM1e (crust). (b) is for IUFSU (core) + TM1 (crust). (c) is for TM1e (core) + TM1 (crust).

are more sensitive to the choice of P_D in the set of $n = 0$. Increasing the number of additional data points can effectively reduce this sensitivity. Similar behaviors are also observed in the other two combinations of the crust and core EOSs.

The effects of changes in n and P_D on the tidal deformability are mediated through their impact on $y(r)$. To be more specific, the impact on $y(r)$ is caused by changes in the sound speed squared $c_s^2 = \partial P / \partial \varepsilon$ in the crust-core connection region, which can be seen in Eq. (5). The partial derivative term $\partial P / \partial \varepsilon$ in $Q(r)$ appears in the denominator and must satisfy $\partial P / \partial \varepsilon \leq 1$ due to causality constraints. Consequently, even slight variations in this term can lead to significant changes in $y(r)$ as shown in the insets of Fig. 4, thereby influencing the final value of y_R . By increasing the number of additional data points, we can reduce the magnitude of changes in $\partial P / \partial \varepsilon$, which in turn decreases the sensitivity to the choice P_D .

B. Crossover connection

In this section, we conduct a regularized calculation to generate a crossover EOS that bridges the inner crust and core segments. We employ the regularized form as described in [47] for the energy density in the connection region, which is expressed as

$$\varepsilon(P) = \frac{1}{2} \left[1 + \tanh \left(\frac{P - P_C}{\Delta P} \right) \right] \varepsilon_{\text{core}}(P) + \frac{1}{2} \left[1 - \tanh \left(\frac{P - P_C}{\Delta P} \right) \right] \varepsilon_{\text{crust}}(P). \quad (16)$$

Here, P_C indicates the critical pressure at which the crust-core phase transition occurs, and ΔP is a parameter used to control the extent of the connection region. To ensure a smooth connection of the crossover EOS to the original crust and core segments, we employ the regularized form given in Eq. (16) until the relative difference in the energy density ε is less than 10^{-3} at both ends of the connection region.

In Fig. 5, we present several profiles of the crossover-connection EOSs. The original crust and core segments are distinguished by thicker lines. To investigate the effects of P_C and ΔP , we consider two critical pressure values ($P_C = 0.25$ and 0.30 MeV/fm 3) along with three distinct ΔP values

($\Delta P = 0.002, 0.005$, and 0.010 MeV/fm 3). The curves with $\Delta P = 0.002$ MeV/fm 3 as shown by the black lines are closer to a first-order phase transition, in which sufficient data points are still included to ensure a smooth change in the sound speed squared. As ΔP increases, the crossover EOS between the crust and core segments becomes smoother, and the crossover region expands.

In Fig. 6, we display the mass-radius relations of neutron stars using the EOSs with the crossover connections. The neutron-star radii are shown to be insensitive to the value of ΔP . Regarding the influence of P_C , it is seen that massive neutron stars exhibit almost no difference in their radii, whereas canonical neutron stars with masses around $1.4 M_\odot$ show small differences in radii, as illustrated in the insets of Fig. 6. The radii with $P_C = 0.25$ MeV/fm 3 (solid lines) are slightly smaller than those with $P_C = 0.30$ MeV/fm 3 (dashed lines). In the three combinations of the crust and core EOSs shown in Fig. 6, the influences of ΔP and P_C on the mass-radius relations follow a similar trend.

In Fig. 7, we show the tidal Love number k_2 (top panels) and the dimensionless tidal deformability Λ (middle panels) as a function of the neutron-star mass M . These results are obtained using the crossover-connection EOSs shown in Fig. 5. For the sets with the same P_C , the $k_2 - M$ curves do not exhibit significant divergence. However, between the sets with $P_C = 0.25$ MeV/fm 3 (solid lines) and $P_C = 0.30$ MeV/fm 3 (dashed lines), small differences can be observed, as illustrated in the insets of Fig. 7(a-1), (b-1), (c-1). In each combination of the crust and core EOSs, all curves of tidal deformability Λ almost completely overlap. Furthermore, the largest difference in $\Lambda_{1.4}$ within one EOS combination is found to be less than 2, as shown in the insets. In Fig. 7(a-3), (b-3), (c-3), we show the $y(r)$ profiles for a $1.4 M_\odot$ neutron star obtained using the crossover-connection EOSs. The $y(r)$ curves for the three EOS combinations exhibit a similar trend. All curves practically coincide in the core region. Small differences appear only within the crust-core connection region, as shown in the insets. The influence of ΔP is almost negligible, whereas the critical pressure P_C yields a visible distinction on the $y(r)$ curves. However, when the $y(r)$ curves extend beyond the crossover region, the curves with different P_C get closer, and ultimately result in almost identical values of y_R . We find that the differences in the tidal deformability of a $1.4 M_\odot$ neutron

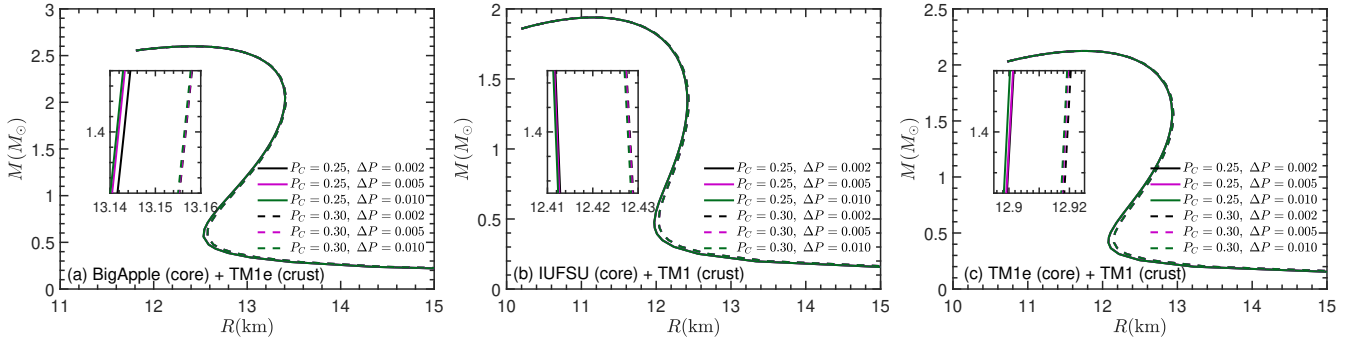


FIG. 6. Mass-radius relations predicted by the crossover-connection EOSs shown in Fig. 5. The insets show more details for canonical neutron stars with masses around $1.4 M_{\odot}$.

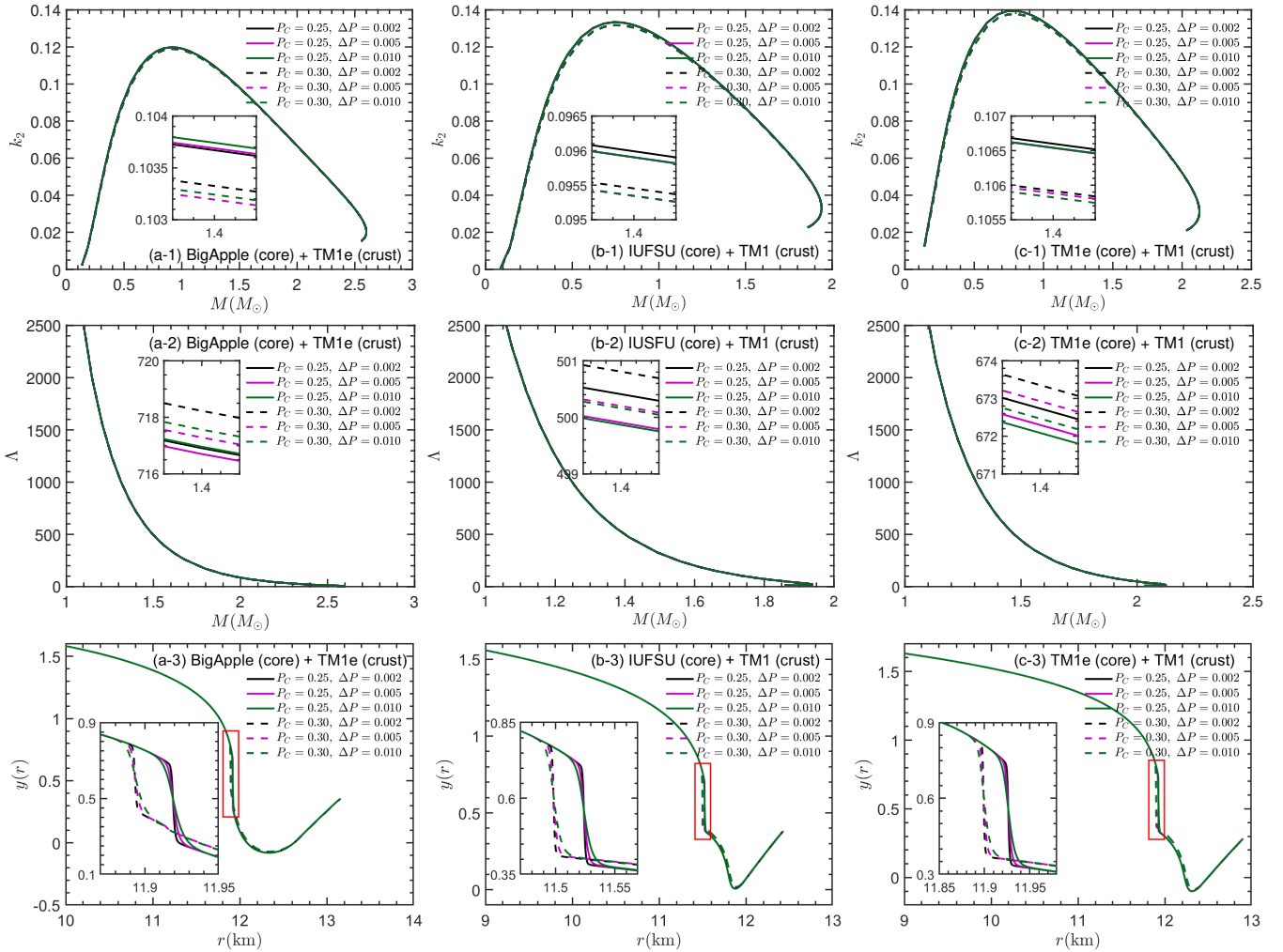


FIG. 7. (a,b,c-1) Love number k_2 and (a,b,c-2) tidal deformability Λ as a function of the neutron-star mass M predicted by the crossover-connection EOSs shown in Fig. 5. The insets show more details for canonical neutron stars with masses around $1.4 M_{\odot}$. (a,b,c-3) The $y(r)$ profiles as given in Eq. (4) for a $1.4 M_{\odot}$ neutron star. The insets show the results in the crossover connection region.

star ($\Lambda_{1.4}$) obtained using the crossover-connection EOSs are very small, which are much smaller than those obtained using the direct-connection EOSs (see Table I, II, III). This implies that the crossover connection provides more stable results of $\Lambda_{1.4}$ than the direct connection.

C. Segmented method

In the direct and crossover connection procedures described above, we first construct an entire EOS data table, and then

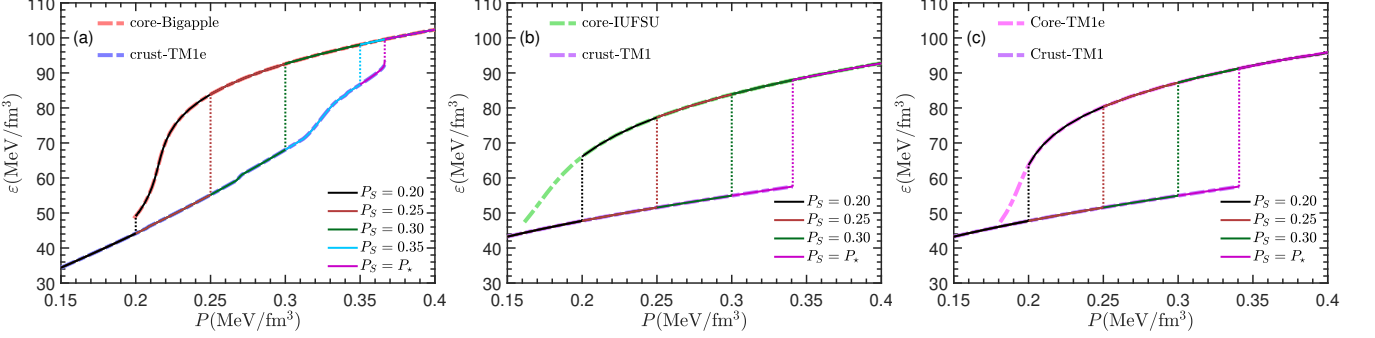


FIG. 8. The EOS profiles in the segmented method. The crust-core transition is assumed to occur at P_S , which is set to different values. The case of $P_S = P_*$ corresponds to the direct connection case with $n = 0$ and $P_D = P_*$, where the inner crust EOS is completely accessed. (a) shows the results for the BigApple (core) + TM1e (crust). (b) is for the IUFSU (core) + TM1 (crust). (c) is for the TM1e (core) + TM1 (crust).

continuously solve the TOV equation from the center to the surface of a neutron star. However, when the discontinuity at the crust-core interface is like a first-order phase transition, the sound speed squared $c_s^2 = \partial P / \partial \varepsilon$ drops close to zero, due to the same pressure but different energy densities between the two phases. The presence of $c_s^2 \simeq 0$ in the denominator of Eq. (5) may lead to difficulty in solving the equation and induce uncertainties in the prediction of the tidal deformability. In order to overcome these difficulties, we solve the TOV equation in segments, employing appropriate matching conditions at the crust-core interface. This procedure is referred to as the segmented method in the present work. We note that appropriate matching conditions should be imposed to ensure continuity and consistency between the crust and core regions.

At the crust-core interface, the pressure is continuous,

$$P_{\text{core}}^{\text{tr}} = P_{\text{crust}}^{\text{tr}} = P_S, \quad (17)$$

while the energy density must monotonically decrease,

$$\varepsilon_{\text{core}}^{\text{tr}} \geq \varepsilon_{\text{crust}}^{\text{tr}}. \quad (18)$$

We denote the radius and enclosed mass at the crust-core transition point inside the neutron star by,

$$\begin{aligned} r_{\text{core}}^{\text{tr}} &= r_{\text{crust}}^{\text{tr}} = r_S, \\ M_{\text{core}}^{\text{tr}} &= M_{\text{crust}}^{\text{tr}} = M_S. \end{aligned} \quad (19)$$

According to Eq. (4) with $c_s^2 \simeq 0$, the matching condition of $y(r)$ at the crust-core interface is expressed as [48, 58]

$$y_{\text{crust}}^{\text{tr}} = y_{\text{core}}^{\text{tr}} - \frac{4\pi r_S^3 (\varepsilon_{\text{core}}^{\text{tr}} - \varepsilon_{\text{crust}}^{\text{tr}})}{M_S}. \quad (20)$$

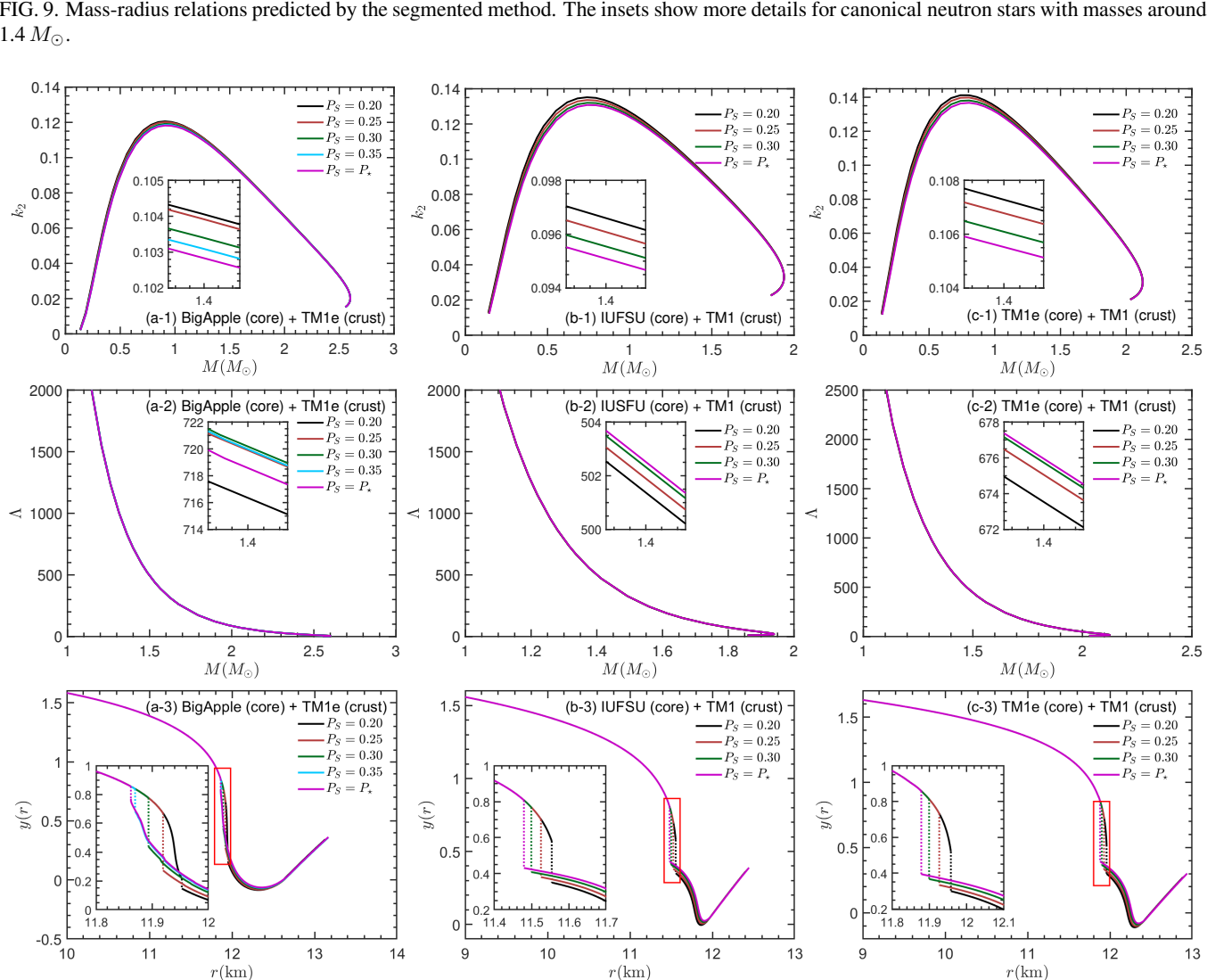
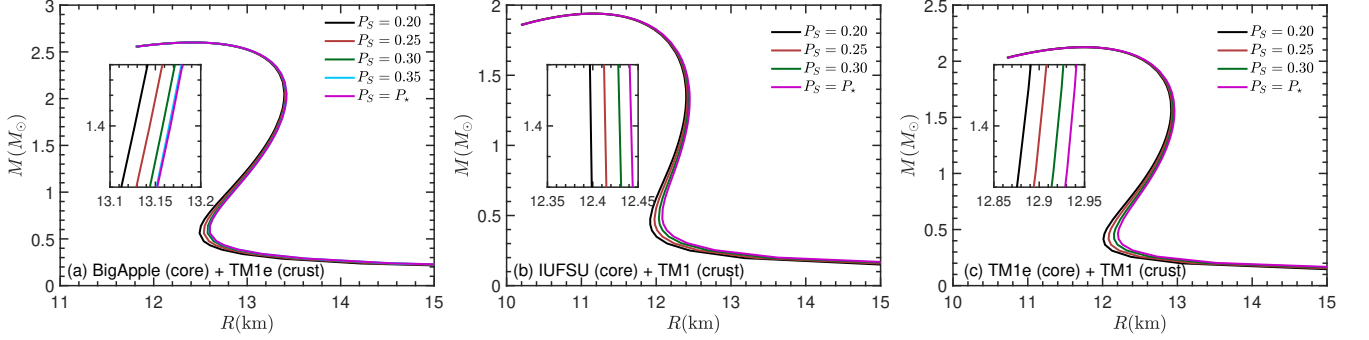
The advantage of the segmented method is that no additional modifications are made to the original crust and core EOS data. A critical parameter in this method is the transition pressure P_S , where the crust-core transition is assumed to occur. We compare results for $P_S = 0.20, 0.25, 0.30, 0.35 \text{ MeV/fm}^3$ and P_* in the segmented method.

In Fig. 8, we show the EOS profiles in the segmented method with various P_S values. The core and crust segments

are connected by a vertical dotted line, analogous to the characteristics of a first-order phase transition. We note that the critical pressures P_* of the TM1 and TM1e models are about 0.341 and 0.366 MeV/fm^3 , respectively. Consequently, the highest P_S shown in Figs. 8(b) and 8(c) with the TM1 crust is $P_* = 0.341 \text{ MeV/fm}^3$, while any $P_S > P_*$ (e.g., $P_S = 0.35 \text{ MeV/fm}^3$) is excluded.

By solving the TOV equation in segments, we obtain the properties of neutron stars. In Fig. 9, we present the mass-radius relations predicted by the segmented method. It is noteworthy that changing the value of P_S is equivalent to altering the crust-core transition point. This alteration does not significantly affect the radii of neutron stars, especially for massive stars. There are small differences observed in the radii of canonical neutron stars with masses around $1.4 M_\odot$, as shown in the insets. It is seen that with increasing P_S , the radius of a $1.4 M_\odot$ neutron star slightly increases, while the largest difference in $R_{1.4}$ within one EOS combination is less than 0.05 km (see Table I, II, III).

In Fig. 10, we show the tidal Love number k_2 (top panels) and the dimensionless tidal deformability Λ (middle panels) as a function of the neutron-star mass M . These results are obtained using the segmented method. The k_2 values corresponding to different P_S exhibit slight variations for massive stars. As the neutron-star mass decreases, the differences in k_2 among various P_S increase and reach a maximum value at $M \approx 0.8 M_\odot$. The insets provide more details for canonical neutron stars with masses around $1.4 M_\odot$. It is shown that the increase in k_2 is negatively correlated with the increase in P_S . This implies that an earlier crust-core transition results in a smaller k_2 , which is consistent with the behavior observed in Fig. 7. For the tidal deformability Λ , there is no significant difference among various values of P_S . According to Eq. (2), for a neutron star with a certain mass, both the love number k_2 and the radius R affect its tidal deformability Λ . With increasing P_S , the decrease in k_2 can mostly offset the increase in the radius R , and as a result, no obvious dependence on P_S is observed in Λ . In Fig. 10(a,b,c-3), we show the $y(r)$ profiles for a $1.4 M_\odot$ neutron star obtained using the segmented method. The $y(r)$ curves for the three EOS combinations exhibit a similar trend. All curves are indistinguishable in the core region. When the crust-core transition occurs at r_S (i.e.,



$P|_{r=r_S} = P_S$), a finite drop in the $y(r)$ profile appears and is indicated by a vertical dotted line, as described in Eq. (20). The dependence on P_S can be observed in the insets. As r increases, the differences in $y(r)$ among various P_S gradually decrease, and ultimately reach almost identical values of y_R .

Compared to the direct connection procedure, the uncertainty of Λ in the segmented method is relatively small. This is because the fluctuation of the sound speed around the crust-core transition does not affect the results in the segmented method, whereas it introduces more uncertainties in the tidal deforma-

TABLE I. Properties of a $1.4 M_{\odot}$ neutron star obtained using the direct connection procedure, crossover connection procedure, and segmented method. $\Delta R_{1.4}$, Δk_2 , and $\Delta \Lambda_{1.4}$ represent the discrepancies between the direct/crossover connection and the segmented method. The results of the direct connection are compared with those for $P_S = P_*$, and the results of the crossover connection are compared with those for $P_S = P_C$. The results in this table are obtained with the BigApple (core) + TM1e (crust) combination.

EOS	BigApple (core) + TM1e (crust)							
	P_D	n	$R_{1.4}$ (km)	k_2	$\Lambda_{1.4}$	$\Delta R_{1.4}$ (km)	Δk_2	$\Delta \Lambda_{1.4}$
Direct connection	P_*	0	13.166	0.0983	685.4	-0.001	-0.0045	-33.1
		0	13.166	0.0997	695.7	-0.001	-0.0031	-22.8
	P_I	1	13.166	0.1020	711.2	-0.001	-0.0008	-7.3
		2	13.166	0.1025	714.7	-0.001	-0.0003	-3.8
		0	13.166	0.1004	700.6	-0.001	-0.0024	-17.9
	P_{II}	1	13.166	0.1024	714.0	-0.001	-0.0004	-4.5
		2	13.166	0.1027	716.5	-0.001	-0.0001	-2.0
		0	13.166	0.1009	704.0	-0.001	-0.0019	-14.5
	P_{III}	1	13.166	0.1025	715.1	-0.001	-0.0003	-3.4
		2	13.166	0.1028	717.2	-0.001	0	-1.3
		0	13.166	0.1014	707.5	-0.001	-0.0014	-11.0
Crossover connection	P_C (MeV/fm ³)	P_*	13.166	0.1028	717.3	-0.001	0	-1.2
		0.002	13.143	0.1037	716.9	-0.001	-0.0002	-2.9
		0.25	13.142	0.1037	716.7	-0.002	-0.0002	-3.1
		0.010	13.141	0.1037	717.0	-0.003	-0.0002	-2.8
		0.002	13.157	0.1033	718.2	-0.001	-0.0001	-1.9
		0.30	13.157	0.1032	717.3	-0.001	-0.0002	-2.8
		0.010	13.157	0.1032	717.6	-0.001	-0.0002	-2.5
		0.20	13.127	0.1041	716.2			
		0.25	13.144	0.1039	719.8			
		0.30	13.158	0.1034	720.1			
Segmented method	P_S (MeV/fm ³)	0.35	13.165	0.1031	719.9			
		P_*	13.167	0.1028	718.5			

bility for the direct connection procedure. Furthermore, when constructing nonunified EOS, the crust-core transition point cannot be accurately determined. This means that the choice of P_S involves a small degree of arbitrariness. Therefore, the values of P_S inevitably introduce some uncertainty into the predictions of neutron stars. In particular, the tidal deformability Λ is relatively sensitive to the crust-core connection. Our results show that the segmented method yields significantly smaller uncertainties than the direct-connection procedure.

We present several properties of a $1.4 M_{\odot}$ neutron star in Tables I, II, III with three combinations of the crust and core EOSs, respectively. The results are obtained using the direct connection procedure, crossover connection procedure, and segmented method. When using nonunified EOSs constructed by the direct connection, it is found that the radius of a $1.4 M_{\odot}$ neutron star $R_{1.4}$ is insensitive to the connection details characterized by the parameters P_D and n . In contrast, the tidal deformability $\Lambda_{1.4}$ is rather sensitive to variations of P_D and n . Particularly, the results of $\Delta \Lambda_{1.4}$ with $n = 0$ are much larger than those in other cases. This is because no additional

data points are added to the connection segment to smooth the EOS in the case of $n = 0$. Increasing n can reduce the differences in tidal deformabilities to a limited extent. For the combinations of IUFSU (core) + TM1 (crust) and TM1e (core) + TM1 (crust), even with $n = 2$, the resulting values of $\Lambda_{1.4}$ still differ markedly from those of the segmented method. The results obtained using the EOSs constructed by the crossover connection procedure are close to those obtained using the segmented method. The resulting values of $\Lambda_{1.4}$ are not very sensitive to the changes of P_C and ΔP in the crossover connection procedure. Compared to the direct and crossover connection procedures, the segmented method provides consistent estimates for $\Lambda_{1.4}$, and the results are not very sensitive to the changes of P_S in the segmented method.

IV. SUMMARY

In this work, we conducted a detailed study on the impact of the crust-core connection procedure when constructing a nonunified EOS for neutron stars, where the crust and core

TABLE II. The same as Table I but for the IUFSU (core) + TM1 (crust) combination.

EOS	IUFSU (core) + TM1 (crust)							
	P_D	n	$R_{1.4}$ (km)	k_2	$\Lambda_{1.4}$	$\Delta R_{1.4}$ (km)	Δk_2	$\Delta \Lambda_{1.4}$
Direct connection	P_\star	0	12,441	0.0757	399.0	-0.002	-0.0194	-101.8
		0	12,443	0.0760	401.1	0	-0.0191	-99.7
	P_I	1	12,443	0.0782	412.8	0	-0.0169	-88.0
		2	12,443	0.0836	440.8	0	-0.0115	-60.0
		0	12,445	0.0763	403.0	+0.002	-0.0188	-97.8
	P_{II}	1	12,444	0.0794	419.1	+0.001	-0.0157	-81.7
		2	12,444	0.0841	444.0	+0.001	-0.0110	-56.8
		0	12,447	0.0766	404.7	+0.004	-0.0185	-96.1
	P_{III}	1	12,446	0.0801	422.9	+0.003	-0.0150	-77.9
		2	12,446	0.0842	444.8	+0.003	-0.0109	-56.0
		0	12,448	0.0769	406.3	+0.005	-0.0182	-94.5
	P_Δ	1	12,447	0.0803	424.5	+0.004	-0.0148	-76.3
		2	12,446	0.0840	444.0	+0.003	-0.0111	-56.8
Crossover connection	P_C	ΔP (MeV/fm ³)	$R_{1.4}$ (km)	k_2	$\Lambda_{1.4}$	$\Delta R_{1.4}$ (km)	Δk_2	$\Delta \Lambda_{1.4}$
	0.25	0.002	12,412	0.0959	499.9	-0.002	-0.0007	+0.2
		0.005	12,412	0.0959	499.9	-0.002	-0.0007	+0.2
		0.010	12,412	0.0960	500.4	-0.002	-0.0006	+0.7
	0.30	0.002	12,428	0.0953	500.1	-0.002	-0.0003	-0.5
		0.005	12,428	0.0953	500.2	-0.002	-0.0003	-0.4
		0.010	12,428	0.0954	500.8	-0.002	-0.0002	+0.2
	Segmented method	P_S (MeV/fm ³)	$R_{1.4}$ (km)	k_2	$\Lambda_{1.4}$	$\Delta R_{1.4}$ (km)	Δk_2	$\Delta \Lambda_{1.4}$
		0.20	12,399	0.0966	499.7			
		0.25	12,414	0.0961	500.2			
		0.30	12,430	0.0956	500.6			
		P_\star	12,443	0.0951	500.8			

segments are obtained within different models. Generally, a finite energy density discontinuity is often present in a nonunified EOS around the crust-core transition, which may induce uncertainties in the prediction of the tidal deformability. We considered three types of connection procedures to treat this discontinuity. The first one, i.e., the direct connection procedure, adopts the Newton interpolation method to directly connect the inner crust and core segments. The second one, i.e., the crossover connection procedure, employs the regularized calculation to generate a crossover EOS between the inner crust and core segments. The third one, i.e., the segmented method, solves the TOV equation separately inside the crust and core regions, while appropriate matching conditions are imposed at the crust-core interface.

Our results indicate that the mass-radius relations of neutron stars are almost unaffected by the details of the connection procedure. However, tidal deformabilities obtained using different connection procedures may have some uncertainties. For a canonical $1.4 M_\odot$ neutron star, uncertainties in the tidal deformability $\Lambda_{1.4}$ from different connection procedures can exceed 20%. This is because the fluctuation of the sound speed around the crust-core transition can significantly affect the results of tidal deformabilities. Among the three types of connection procedures considered in the present work, the direct connection yields significantly larger uncer-

tainties in $\Lambda_{1.4}$ than the crossover connection and segmented method. To avoid the influence caused by the fluctuation of the sound speed, we employ the segmented method, in which the TOV equation is solved in segments, with appropriate matching conditions at the crust-core interface. The advantage of the segmented method is that no additional modifications are made to the original crust and core EOS data. As a result, the uncertainties in the segmented method are much smaller than those in the direct connection procedure. On the other hand, the crossover connection introduces an additional EOS segment, which is generated using a regularized calculation and bridges the inner crust and core segments. It is found that both the crossover connection and segmented method can provide stable results for the tidal deformability. We emphasize that when employing a nonunified EOS to study neutron-star properties, especially the tidal deformability, special attention should be paid to the crust-core connection procedure.

V. ACKNOWLEDGMENTS

This work was partially supported by the National Natural Science Foundation of China under Grant Nos. 12175109 and 12475149, and by Guangdong Basic and Applied Basic Research Foundation under Grant No. 2024A1515010911.

TABLE III. The same as Table I but for the TM1e (core) + TM1 (crust) combination.

EOS	TM1e (core) + TM1 (crust)							
	P_D	n	$R_{1.4}$ (km)	k_2	$\Lambda_{1.4}$	$\Delta R_{1.4}$ (km)	Δk_2	$\Delta \Lambda_{1.4}$
Direct connection	P_\star	0	12.935	0.0796	509.0	0	-0.0259	-165.8
		0	12.936	0.0800	511.9	+0.001	-0.0255	-162.9
	P_1	1	12.936	0.0827	529.1	+0.001	-0.0228	-145.7
		2	12.936	0.0897	574.1	+0.001	-0.0158	-100.7
		0	12.938	0.0803	513.9	+0.003	-0.0252	-160.9
	P_{II}	1	12.937	0.0840	537.5	+0.002	-0.0215	-137.3
		2	12.937	0.0903	578.0	+0.002	-0.0152	-96.8
		0	12.940	0.0804	515.2	+0.005	-0.0251	-159.6
	P_{III}	1	12.938	0.0845	541.3	+0.003	-0.0210	-133.5
		2	12.938	0.0902	577.7	+0.003	-0.0153	-97.1
		0	12.942	0.0814	522.1	+0.007	-0.0241	-152.7
	P_Δ	1	12.940	0.0858	549.7	+0.005	-0.0197	-125.1
		2	12.939	0.0905	580.1	+0.004	-0.0150	-94.7
Crossover connection	P_C (MeV/fm ³)	ΔP (MeV/fm ³)	$R_{1.4}$ (km)	k_2	$\Lambda_{1.4}$	$\Delta R_{1.4}$ (km)	Δk_2	$\Delta \Lambda_{1.4}$
	0.25	0.002	12.899	0.1065	672.1	-0.003	-0.0003	-1.8
		0.005	12.900	0.1065	672.3	-0.002	-0.0003	-1.6
		0.010	12.900	0.1066	672.7	-0.002	-0.0002	-1.2
	0.30	0.002	12.918	0.1058	672.5	-0.002	-0.0003	-2.1
		0.005	12.919	0.1059	672.9	-0.001	-0.0002	-1.7
		0.010	12.919	0.1059	673.4	-0.001	-0.0002	-1.2
Segmented method	P_S (MeV/fm ³)		$R_{1.4}$ (km)	k_2	$\Lambda_{1.4}$	$\Delta R_{1.4}$ (km)	Δk_2	$\Delta \Lambda_{1.4}$
	0.20		12.884	0.1073	672.4			
		0.25	12.902	0.1068	673.9			
		0.30	12.920	0.1061	674.6			
	P_\star		12.935	0.1055	674.8			

[1] H. Koehn, H. Rose, P. T. H. Pang, R. Somasundaram, B. T. Reed, I. Tews, A. Abac, O. Komoltsev, N. Kunert, A. Kurkela, M. W. Coughlin, B. F. Healy, and T. Dietrich, *Physical Review X* **15**, 021014 (2025).

[2] K. Chatzioannou, H. T. Cromartie, S. Gandolfi, I. Tews, D. Radice, A. W. Steiner, and A. L. Watts, *Rev. Mod. Phys.* **97**, 045007 (2025).

[3] S. Ascenzi, V. Graber, and N. Rea, *Astroparticle Physics* **158**, 102935 (2024).

[4] B. P. Abbott, R. Abbott, T. D. Abbott, M. R. Abernathy, F. Acernese, K. Ackley, C. Adams, T. Adams, P. Addesso, *et al.* (LIGO Scientific Collaboration and Virgo Collaboration), *Physical Review Letters* **116**, 061102 (2016).

[5] B. P. Abbott, R. Abbott, T. Abbott, F. Acernese, K. Ackley, C. Adams, T. Adams, P. Addesso, R. Adhikari, V. B. Adya, *et al.*, *Phys. Rev. Lett.* **119**, 161101 (2017).

[6] B. P. Abbott, R. Abbott, T. Abbott, F. Acernese, K. Ackley, C. Adams, T. Adams, P. Addesso, R. X. Adhikari, V. B. Adya, *et al.*, *Phys. Rev. Lett.* **121**, 161101 (2018).

[7] F. J. Fattoyev, J. Piekarewicz, and C. J. Horowitz, *Phys. Rev. Lett.* **120**, 172702 (2018).

[8] E. R. Most, L. R. Weih, L. Rezzolla, and J. Schaffner-Bielich, *Phys. Rev. Lett.* **120**, 261103 (2018).

[9] P. Landry, R. Essick, and K. Chatzioannou, *Physical Review D* **101**, 123007 (2020).

[10] K. Chatzioannou, *General Relativity and Gravitation* **52**, 109 (2020).

[11] Z. Arzoumanian, A. Brazier, S. Burke-Spolaor, *et al.*, *Astrophys. J. Supp.* **235**, 37 (2018).

[12] J. Antoniadis, P. C. C. Freire, N. Wex, *et al.*, *Science* **340**, 1233232 (2013).

[13] E. Fonseca, H. T. Cromartie, T. T. Pennucci, *et al.*, *Astrophys. J. Lett.* **915**, L12 (2021).

[14] M. C. Miller, F. K. Lamb, A. J. Dittmann, S. Bogdanov, Z. Arzoumanian, K. C. Gendreau, S. Guillot, A. Harding, W. Ho, J. M. Lattimer, *et al.*, *Astrophys. J. Lett.* **887**, L24 (2019).

[15] T. E. Riley, A. L. Watts, S. Bogdanov, P. S. Ray, R. M. Ludlam, S. Guillot, Z. Arzoumanian, C. L. Baker, A. V. Bilous, D. Chakrabarty, *et al.*, *Astrophys. J. Lett.* **887**, L21 (2019).

[16] M. C. Miller, F. K. Lamb, A. J. Dittmann, S. Bogdanov, Z. Arzoumanian, K. C. Gendreau, S. Guillot, W. C. G. Ho, J. M. Lattimer, M. Loewenstein, *et al.*, *Astrophys. J. Lett.* **918**, L28 (2021).

[17] T. E. Riley, A. L. Watts, P. S. Ray, S. Bogdanov, S. Guillot, S. M. Morsink, A. V. Bilous, Z. Arzoumanian, D. Choudhury, J. S. Deneva, *et al.*, *Astrophys. J. Lett.* **918**, L27 (2021).

[18] N. Chamel and P. Haensel, *Living Rev. Relativ.* **11**, 10 (2008).

[19] J. M. Lattimer and M. Prakash, *Phys. Rep.* **621**, 127 (2016), memorial Volume in Honor of Gerald E. Brown.

[20] M. Oertel, M. Hempel, T. Klähn, and S. Typel, *Reviews of Modern Physics* **89**, 015007 (2017).

[21] D. G. Ravenhall, C. J. Pethick, and J. R. Wilson, *Phys. Rev. Lett.* **50**, 2066 (1983).

[22] S. S. Avancini, D. P. Menezes, M. D. Alloy, J. R. Marinelli, M. M. W. Moraes, and C. Providência, *Phys. Rev. C* **78**, 015802 (2008).

[23] S. S. Bao and H. Shen, *Phys. Rev. C* **89**, 045807 (2014).

[24] F. Weber, *Progress in Particle and Nuclear Physics* **54**, 193 (2005).

[25] A. Ohnishi, D. Jido, T. Sekihara, and K. Tsubakihara, *Physical Review C* **80**, 038202 (2009).

[26] T. Khunjua, K. Klimenko, and R. Zhokhov, *Symmetry* **11** (2019), 10.3390/sym11060778.

[27] P. Yue and H. Shen, *Physical Review C* **77**, 045804 (2008).

[28] P. Char and S. Banik, *Physical Review C* **90**, 015801 (2014).

[29] D. Kundu, V. B. Thapa, and M. Sinha, *Physical Review C* **107**, 035807 (2023).

[30] F. Yang and H. Shen, *Physical Review C* **77**, 025801 (2008).

[31] D. Logoteta, *Universe* **7** (2021), 10.3390/universe7110408.

[32] Z.-H. Tu and S.-G. Zhou, *The Astrophysical Journal* **925**, 16 (2022).

[33] K. X. Huang, J. N. Hu, Y. Zhang, and H. Shen, *Astrophys. J.* **935**, 88 (2022).

[34] E. Annala, T. Gorda, A. Kurkela, J. Nättälä, and A. Vuorinen, *Nature Physics* **16**, 907 (2020).

[35] X. H. Wu and H. Shen, *Phys. Rev. C* **99**, 065802 (2019).

[36] M. Ju, J. N. Hu, and H. Shen, *Astrophys. J.* **923**, 250 (2021).

[37] K. Huang, J. Hu, Y. Zhang, and H. Shen, *Nuclear Physics Review* **39**, 135 (2022).

[38] C.-J. Xia, T. Maruyama, N. Yasutake, and T. Tatsumi, *Physical Review D* **110**, 114024 (2024).

[39] F. Douchin and P. Haensel, *Astronomy & astrophysics* **380**, 151 (2001).

[40] H. Shen, *Phys. Rev. C* **65**, 035802 (2002).

[41] T. Miyatsu, S. Yamamuro, and K. Nakazato, *Astrophys. J.* **777**, 4 (2013).

[42] A. Fantina, N. Chamel, J. Pearson, and S. Goriely, *Astronomy & astrophysics* **559**, A128 (2013).

[43] F. Gulminelli and A. R. Raduta, *Physical Review C* **92**, 055803 (2015).

[44] M. Fortin, C. Providência, A. R. Raduta, F. Gulminelli, J. L. Zdunik, P. Haensel, and M. Bejger, *Phys. Rev. C* **94**, 035804 (2016).

[45] F. Ji, J. N. Hu, S. S. Bao, and H. Shen, *Phys. Rev. C* **100**, 045801 (2019).

[46] M. Gasca and T. Sauer, *Advances in Computational Mathematics* **12**, 377 (2000).

[47] M. G. Alford, S. P. Harris, and P. S. Sachdeva, *Astrophys. J.* **847**, 109 (2017).

[48] S. Postnikov, M. Prakash, and J. M. Lattimer, *Phys. Rev. D* **82**, 024016 (2010).

[49] F. Fattoyev, C. Horowitz, J. Piekarewicz, and B. Reed, *Phys. Rev. C* **102**, 065805 (2020).

[50] F. J. Fattoyev, C. J. Horowitz, J. Piekarewicz, and G. Shen, *Phys. Rev. C* **82**, 055803 (2010).

[51] M. Dutra, O. Lourenço, S. Avancini, B. V. Carlson, A. Delfino, D. Menezes, C. Providência, S. Typel, and J. Stone, *Phys. Rev. C* **90**, 055203 (2014).

[52] S. S. Bao, J. N. Hu, Z. W. Zhang, and H. Shen, *Phys. Rev. C* **90**, 045802 (2014).

[53] H. Shen, F. Ji, J. N. Hu, and K. Sumiyoshi, *Astrophys. J.* **891**, 148 (2020).

[54] S. S. Bao and H. Shen, *Phys. Rev. C* **91**, 015807 (2015).

[55] G. Baym, H. A. Bethe, and C. J. Pethick, *Nucl. Phys. A* **175**, 225 (1971).

[56] J. R. Oppenheimer and G. M. Volkoff, *Physical Review* **55**, 374 (1939).

[57] T. Hinderer, *The Astrophysical Journal* **677**, 1216 (2008).

[58] S. Han and A. W. Steiner, *Physical Review D* **99**, 083014 (2019).